

# A 3D Meso-Scale Solidification Model for Metallic Alloy Using A Volume Average Approach

Yi Feng<sup>1</sup>, A.B. Phillion<sup>1\*</sup>

<sup>1</sup> Department of Materials Science and Engineering  
McMaster University, Hamilton, ON, Canada, L8S 4L7  
\*Email: philliab@mcmaster.ca

**Keywords:** solidification; hot tearing; semi-solid; steel; segregation; continuous casting

## ABSTRACT

A 3D discrete-element model has been developed to simulate the solidification of steel at the meso-scale. The domain consists of a set of equiaxed grains along with the liquid channels, where the fully solid grain shape is given by a modified Voronoi diagram. The primary solidification and peritectic transformation within each grain is modeled using a volume average approach. Thus, phase evolution within the semisolid domain with either dendritic or globular microstructure can be predicted depending on different cooling rates. The coalescence phenomenon between grains is considered at the end of solidification using Bulatov's approach for estimating interfacial energy. It is seen that only 0.9% of the grains are attractive based on their orientations, significantly depressing final-stage solidification. The results demonstrate the ability of this modelling approach to investigate morphology transitions during the solidification of alloys having a range of composition from non-peritectic to hyper-peritectic. The influences of grain size, carbon content and cooling rate on the solidification behavior are also investigated. Further, it is shown that the semi-solid morphology of hypo-peritectic steel alloys at high solid fraction contains very thin liquid channels, in comparison to other compositions, when the peritectic transformation occurs thus increasing the hot tearing susceptibility. This meso-scale model will be used in conjunction with semi-solid fluid flow and deformation simulations for multi-physics modelling of solidification.

## 1. INTRODUCTION

The occurrence of transverse cracks on the surface of advanced high strength steel slabs remains a problem for the steelmaking industry, despite many decades of research. These cracks are often found along abnormally large austenite grains, known as "blown grains" [1] that form just below the oscillation marks [2]. It is thought that the blown grains act as precursors to the occurrence of micro cracks, namely hot tears, during the initial solidification [3-5] that then grow into macroscale transverse cracks [6]. Hot tears usually form in the mushy state at high solid fraction where a thin liquid film exists around solid grains [7]. These cracks develop because of the concomitant phenomena of solidification shrinkage and thermo-mechanical deformation acting on the mushy zone when there is not enough liquid feeding [8, 9]. Investigation of the mechanisms behind hot tearing formation provides the knowledge required for reducing the occurrence of this detrimental defect.

Hot tearing criteria offer one approach for predicting the susceptibility of an alloy / process combination to the occurrence of this defect [10-14]. Due to the small length scale of dendritic microstructure, these criteria usually predict hot tearing susceptibility based on a macroscale approach in which the mushy zone is considered as a single phase and average values are used to characterize various properties of the mushy zone. However, hot tearing is a multi-scale and multi-physics problem as microstructure and fluid flow occur at the microscale while stress develops at the macroscale. At present,

none of the criteria are able to predict the strain distribution along grain boundaries that leads to cracking nor consider the coalescence phenomenon between two distinct grains that reduces cracking.

3D meso-scale and multi-physics modelling of solidification offers the possibility to quantitatively predict the localization and initiation of hot tears, thus overcoming the limitation of prior criteria. In this modelling approach, a Voronoi diagram is used to approximate the morphology of solidifying alloys having equiaxed-globular microstructure. Sistaninia *et al.* [15], building on prior work by Mathier *et al.* [16] and Vernede *et al.* [17], developed a 3-D hydromechanical model of the solidification, liquid feeding and mechanical deformation of Al-Cu alloys in the semi-solid state. The results were validated against X-ray tomography images of semi-solid deformation [18]. In addition to the scientific advantages of this modelling approach for understanding the hot tearing phenomena, this approach is highly efficient, enabling multi-physics simulation of hot tearing in only a few hours. Recently, Rajani *et al.* [19, 20] successfully applied this modelling framework to fusion welding process for the aluminum alloy AA6061. The recent results enabled prediction of the effects of external mechanical restraints on deformations within the mushy zone, which were then used to link welding process parameters with the occurrence of hot tearing.

The past uses of the 3D meso-scale and multi-physics models for investigating hot tearing have focused mainly on the equiaxed-globular structure of aluminum alloys. This structure is not applicable for continuously-cast steels alloys having a dendritic microstructure and sometimes exhibiting a peritectic transformation. One approach that has shown success in modelling dendritic structures is the so-called micro-macro solute diffusion approach that accounts for the different length scales present during dendritic solidification. First proposed by Rappaz *et al.* [21], and then formalized as a volume average method by Wang and Beckermann [22], this approach is able to predict phase fraction evolution and the growth of dendrite tips. Recently, the formation of peritectic/eutectic microstructures was added to this approach by Tourret *et al.* [23-25], firstly growing into the liquid phase and then consuming both primary and liquid phases concurrently.

In this study, a 3D meso-scale solidification model of solidifying Fe-C alloys is proposed to investigate late-stage solidification phenomena that lead to hot tearing. This new model allows for the investigation of microstructure morphology transition from individual dendritic grains to a percolated solid network, while permitting a detailed analysis of the evolution in  $\delta$  fraction, dendrite envelope fraction (containing both solid and intra-dendritic liquid phase), and  $\gamma$  fraction (in peritectic grades) at the scale of a single grain. A model [26] that takes into account the five physical parameters of misorientation is used to quantify the grain boundary energies that control the disappearance of the thin liquid films between grains. The influences of alloy composition and casting parameters on the solidification behavior of a representative semi-solid volume element containing 1000 grains is reported.

## 2. MODEL DEVELOPMENT

*2.1 Simulation Domain and Overview of Meso-scale Solidification Model:* The microstructure of semi-solid steel near the meniscus is assumed to consist of a large number of equiaxed dendritic grains having different orientations, and a continuous liquid layer coexisting around the solid structure. To approximate the 3-D microstructure in this region, an unstructured mesh is created based on a Voronoi tessellation [9] of the grain nuclei within a representative volume element, Fig. 1(a), whereby each polygon, Fig. 1(b) represents one grain. The grains are then subdivided into smaller polyhedral sub-elements, Fig. 1(c), which are further divided into many tetrahedral elements with the nucleation site as the summit and the surface of the polyhedral as the base, shown in Fig. 1(d-1). The grain density within the domain is acquired from metallographic analysis and used as a model input parameter.

Solidification is simulated independently for each tetrahedral element using a 1-D volume average method in spherical coordinates as described in Section 2.2. A uniform temperature assumption is applied throughout the domain, nucleation of all grains is assumed to occur simultaneously, and the boundaries of each fully solidified grain correspond to the shape of a Voronoi polygon. To simulate dendritic solidification, the position of the dendrite envelope is tracked, moving from the initial nucleation site at  $t=0$  to the boundary of the Voronoi tessellation. Then, each tetrahedral element is partitioned into different phases depending on the fraction of each phase. As the dendritic morphology indicated in Fig. 1(d-1) cannot be visualized by an unstructured mesh, the model shows the equivalent phase fraction in a geometric sense, Fig. 1(d-2). The bulk solid fraction within the domain is then estimated by summing all of the solid within each tetrahedral element. An example simulation domain,  $125 \text{ mm}^3$  and created using the developed C++ code, is shown in Fig. 1(e). In this domain, the solid fraction is 0.81 and the average size of the equiaxed  $\delta$  grains is  $\sim 500 \text{ }\mu\text{m}$ . Note that the liquid phase represents the sum of both intra-dendritic and extra-dendritic liquid phase for dendritic structure shown in Fig. 1(e); the amount of remaining liquid within each grain is represented by the channel thickness.

*2.2 Solidification Model:* Solidification of the dendritic structure is simulated using a volume average method for multiphase binary systems [23-25, 27]. The occurrence of the peritectic transformation is also included, for relevant chemistries. In the average volume approach, the evolution of the solid/liquid interface cannot be explicitly tracked. Instead the individual phase fractions, i.e. the primary delta  $g_\delta$ , austenite  $g_\gamma$  and liquid  $g_l$  phase fractions are obtained using the model described below. The liquid phase fraction is further distinguished as intra-dendritic  $g_{l\_intra}$  and extra-dendritic liquid  $g_{l\_extra}$ . The dendrite envelope fraction,  $g_g$ , represents the total amount of solid phase as well as the intra-dendritic liquid, i.e.  $g_g = g_\delta + g_\gamma + g_{l\_intra}$ . The main idea of the volume average approach is that the  $\delta$  and/or  $\gamma$  phases nucleate from the center of the grain in an undercooled liquid ( $l$ ) and grow in radial direction until the total element length,  $R$ , is reached, as shown in either Fig. 2(a) or (b). Different zones are used to track the formation and disappearance of various phases; each phase can coexist in multiple zones. As stated previously, temperature is assumed to be uniform and continuously cooling at a given rate. In primary solidification, the  $\delta$  dendrite tip position ( $R^{(1)}$ ) separates zones (0) and (1), as shown in Fig. 2(a1). Zone (0) contains only extra-dendritic liquid ( $g_l^{(0)}$ ) whereas zone (1) contains intra-dendritic liquid ( $g_l^{(1)}$ ) and  $\delta$

phase ( $g_\delta^{(1)}$ ). Zone (2), a combination of  $\delta$  phase ( $g_\delta^{(2)}$ ),  $\gamma$  phase ( $g_\gamma^{(2)}$ ) and intra-dendritic liquid ( $g_l^{(2)}$ ), forms when the  $\gamma$  phase nucleates, eliminating zone (1) as shown in Fig. 2(b1). It is assumed that the peritectic reaction occurs instantaneously, and thus the position of the  $\gamma$  phase tip ( $R^{(2)}$ ) is equal to the position of the primary  $\delta$  dendrite tip ( $R^{(1)}$ ). The dendrite tip position also denotes the edge of the dendrite envelope. The radial growth rate of the dendrite tip is predicted via a kinetic model [28]. The dendrite envelope fraction is calculated as  $g_g = 1 - g_{l\_extra}$ , where  $g_{l\_extra} = g_l^{(0)}$ . Alternatively, it could be calculated as  $g_g = \sum_{i=1}^2 g_\delta^{(i)} + \sum_{i=1}^2 g_\gamma^{(i)} + \sum_{i=1}^2 g_l^{(i)}$ . Note that the superscript indicates the zone that the phase exists. The sum of the volume fractions ( $g$ ) of each phase within a grain is equal to unity, such that  $g_\delta + g_\gamma + g_l = 1$ . Due to the different concentrations of the  $\delta$ ,  $\gamma$  and  $l$  phases, a solute mass balance is considered individually for each phase in each zone, and the solute exchange at the zone boundaries is also included. Note that equal and constant densities are assumed for all phases. For more details on the volume average approach to model dendritic growth, please refer to [22].

Inside each zone,  $\alpha$  and  $\beta$  represent individual arbitrary phases. The average mass conservation of an individual phase and mass exchange over the phase interface are given by

$$\frac{\partial g^\alpha}{\partial t} = \sum_{\alpha/\beta} (S^{\alpha/\beta} v^{\alpha/\beta}), \text{ and} \quad (1)$$

$$v^{\alpha/\beta} + v^{\beta/\alpha} = 0, \quad (2)$$

where  $g^\alpha$  is the volume fraction of an individual phase within each zone,  $v^{\alpha/\beta}$  is the normal velocity of the phase interface on the  $\alpha$  side shown in Fig. 2(a2) as  $v^{\delta/l}$ , and  $S^{\alpha/\beta}$  is the interfacial area concentration, defined as  $A^{\alpha/\beta}/V$ , where  $A^{\alpha/\beta}$  is the interfacial area between the  $\alpha$  and  $\beta$  phases and  $V$  represents the total volume of the domain. Note that phases co-existing in multiple zones are considered to be different phases.

For an individual phase, solute conservation is given as

$$g^\alpha \frac{\partial \langle c^\alpha \rangle^\alpha}{\partial t} = \sum_{\beta(\beta \neq \alpha)} S^{\alpha/\beta} (c^{\alpha/\beta} - \langle c^\alpha \rangle^\alpha) \left( v^{\alpha/\beta} + \frac{D^\alpha}{\ell^{\alpha/\beta}} \right), \text{ and} \quad (3)$$

$$(c^{\alpha/\beta} - c^{\beta/\alpha}) v^{\alpha/\beta} + \frac{D^\alpha}{\ell^{\alpha/\beta}} (c^{\alpha/\beta} - \langle c^\alpha \rangle^\alpha) + \frac{D^\beta}{\ell^{\beta/\alpha}} (c^{\beta/\alpha} - \langle c^\beta \rangle^\beta) = 0, \quad (4)$$

where  $c^{\alpha/\beta}$  represents the solute concentration of the phase interface on the  $\alpha$  side. The concentrations at the  $\delta/l$  or  $\gamma/l$  interface are given by the equilibrium binary phase diagram, the two symbols  $\langle c^\alpha \rangle^\alpha$  and  $\langle c^\beta \rangle^\beta$  represent the average solute concentration in  $\alpha$  and  $\beta$ ,  $\ell^{\alpha/\beta}$  represents the diffusion length in the  $\alpha$  phase, and  $D^\alpha$  and  $D^\beta$  are the solute diffusion coefficient in  $\alpha$  and  $\beta$ . The expressions for the interfacial area concentration  $S^{\alpha/\beta}$  and diffusion length  $\ell^{\alpha/\beta}$  are presented in detail elsewhere [23, 27].

The boundary velocity for zone (1) or zone (2) is equal to the dendrite tip velocity of  $\delta$  or  $\gamma$  growing into the undercooled liquid. This tip velocity is calculated using the KGT model [28],

$$v_n^{(1)} = - \frac{D^l m^{\delta/l} (c^{l/\delta} - c^{\delta/l})}{\pi^2 \Gamma^{\delta/l}} [Iv^{-1}(\Omega^{\delta/l})]^2, \quad (5)$$

where  $v_n^{(1)}$  is the boundary velocity of zone (1),  $m^{\delta/l}$  is the liquidus slope of  $\delta$  phase,  $\Gamma^{\delta/l}$  is the Gibbs-Thompson coefficient, and  $Iv^{-1}$  and  $\Omega^{\delta/l}$  represent the inverse of the Ivantsov function, and solute supersaturation, respectively [22],

$$Iv^{-1}(\Omega^{\delta/l}) = 0.4567 \cdot \left( \frac{\Omega^{\delta/l}}{1-\Omega^{\delta/l}} \right)^{1.195}, \text{ and} \quad (6)$$

$$\Omega^{\delta/l} = \left[ c^{l/\delta} - \langle c^{l(0)} \rangle^{l(0)} \right] / \left[ c^{l/\delta} - c^{\delta/l} \right]. \quad (7)$$

In Eq. (5), (6), and (7)  $l$  and  $\delta$  represent the arbitrary phases  $\alpha$  and  $\beta$ .

The 1-D volume average solidification model is applied to each tetrahedral element, assuming the element height to be the total grain radius,  $R$ , and solute exchange between two neighboring elements is neglected. In this fashion, the variation in individual phases along with the evolution of semi-solid morphology can be predicted at the meso-scale. This model is implemented using a purpose-written C++ code that solves Equations (1)-(7) simultaneously for each phase, within each zone, for each grain. The differential equations are discretized using an explicit difference method, with the term on the left-hand side of the equation being calculated from the values taken from the previous time step. The detailed solution procedure is as follows. First, time is incremented to the next time step. This results in an incremental reduction in temperature and causes the equilibrium concentrations at the interface  $c^{\alpha/\beta}$  to be updated based on the phase diagram. Second,  $v_n^{(i)}$  is calculated based on Eq. (5), and the volume fraction of each zone (zone 0, zone 1, zone 2, ...) is updated. Third,  $S^{\alpha/\beta}$  and  $\rho^{\alpha/\beta}$  are determined, and then  $v^{\alpha/\beta}$  is obtained by combining Eq. (2) and Eq. (4). Subsequently, the concentration at the zone boundary  $c^{\alpha/\beta}$  is calculated via Eq. (4) for phases that co-exist in two zones. Finally, the volume fraction and average concentration of each phase are determined using Eq. (1) and Eq. (3). All of the values for these parameters at the present step are then used as initial conditions for the next time step. Once the volume fraction of each phase has been calculated, the equivalent positions of the various interfaces are determined, in a geometric sense, as shown in Fig. 2(a2) and Fig. 2(b2) to show the structure within the framework of a Voronoi tessellation.

An example of the model results for a single grain is shown in Fig. 3, which predicts the solidification behavior (evolution in the dendrite envelope fraction  $g_g$  and the delta-ferrite fraction  $g_\delta$  as a function of time) of a non-peritectic alloy with 0.07wt.% carbon being cooled at 0.1°C/s and 50°C/s. The results indicate that at 0.1°C/s, a low cooling rate, the kinetics of the dendrite envelope evolution is rather slow. This can be seen by the superposition of the solid fraction and grain fraction curves in Fig. 3(a). At the initial stage of solidification,  $g_g$  increases faster than the solid fraction and a small dendritic structure forms. However, as solidification continues, the solid fraction becomes equal to the dendrite envelope fraction resulting in a final microstructure that is globular. On the other hand, when a cooling rate of 50°C/s is applied to the model, the dendrite envelope grows quite fast until it reaches the maximum grain radius whereas the solid fraction evolves at a much slower rate. The gap between the two curves leads to the formation of a dendritic structure. Thus, during continuous casting, while the dendrite envelopes from neighboring grains may be about to touch, a great amount of liquid remains in the intra-dendritic regions. This is an indication that although the extra-dendritic liquid films may be thin, the remaining intra-dendritic liquid might play an important role in hot tearing susceptibility.

Through this small example it is shown that the use of a volume average method as part of the 3-D mesoscale solidification model is able to predict dendritic structure near the meniscus where the cooling rates are high but will still predict globular grains near the centre of the slab where cooling rates are low.

The formation of the columnar zone is ignored in this study because of the focus on blown grains; it was covered in one of our prior publications [29].

**2.3 Coalescence Criterion:** When two grains with different orientations are about to touch each other, a driving force is needed to determine the non-equilibrium temperature when they will coalesce and form a solid bridge [30].

Solidification of the last liquid film depends on the interfacial energies of the (dry) grain boundary,  $\gamma_{gb}$  and of the solid-liquid interface,  $\gamma_{sl}$  [30]. For a pure metal, the excess free energy of two interfaces approaching each other at the melting temperature deviates from  $\gamma_{sl}$  until it equals  $\gamma_{gb}$  when the liquid channel has completely disappeared. The expression of the excess energy  $\gamma(h)$  as a function of channel width ( $h$ ) at the melting temperature is given by

$$\gamma(h) = 2\gamma_{sl} + (\gamma_{gb} - 2\gamma_{sl})\exp\left(\frac{-h}{\eta}\right), \quad (8)$$

where  $\eta$  represents the thickness of diffuse solid/liquid interface ( $\eta \sim 1-3\text{nm}$ ) [31] (note – coalescence phenomena can only be felt at this length scale). The forces between two grains can be categorized into three cases: attractive ( $\gamma_{gb} < 2\gamma_{sl}$ ), neutral ( $\gamma_{gb} = 2\gamma_{sl}$ ), and repulsive ( $\gamma_{gb} > 2\gamma_{sl}$ ). At other temperatures, the excess free energy  $G(h)$  (per unit area) resulting from supercooled liquid is given by

$$G(h) = (G_l - G_s)h + \gamma(h) = \Delta S_f h \Delta T + \gamma(h), \quad (9)$$

where  $G_l$  and  $G_s$  are the free energy of liquid and solid phase per unit volume,  $\Delta S_f$  represents the volumetric entropy of fusion, and  $\Delta T$  is the undercooling relative to the melting temperature. Rappaz *et al.* [30] combined Equations (8) and (9) to show that stable liquid films will remain between two grains below the equilibrium solidification temperature until a coalescence undercooling ( $\Delta T_b$ ) is reached,

$$\Delta T_b = \frac{\gamma_{gb} - 2\gamma_{sl}}{\Delta S_f \cdot \eta} \quad (10)$$

As can be seen in Eq. (10), the sign of the coalescence undercooling depends on the difference between  $\gamma_{gb}$  and  $\gamma_{sl}$ . In alloys,  $\Delta T_b$ , is also influenced by solute enrichment in the liquid film due to microsegregation. Thus, the coalescence results in a shift downwards of the liquidus line by a certain solute undercooling.

$\gamma_{gb}$  depends critically on the misorientation between two grains. For dendrite arms belonging to the same grain, no misorientation exists and  $\gamma_{gb} = 0$ . In this case, a solid bridge would immediately form between these dendrite arms when they are a few nanometers away as they attract each other. For dendrite arms belonging to different grains,  $\gamma_{gb}$  is influenced by five parameters; three for misorientation between the crystal lattice of the two grains and two for the orientation of the grain boundary plane itself.

The mesoscale solidification model of steel includes the requirement to overcome the thermodynamic barrier to coalescence between neighboring grains in order to predict the gradual formation of grain clusters that are able to withstand deformations applied to the mushy zone. Specifically, Eq. (10) is applied to determine the required undercooling for bridging between two dendritic-equiaxed grains to predict the transient from the isolated solid grains to one coherent solid cluster. The prior work of Sistaninia randomly assigned a single orientation value between  $0^\circ$  and  $90^\circ$  to each grain and then calculated  $\gamma_{gb}$  [8, 16, 17, 31-33] based on a symmetric tilt boundary along [100]. Bulatov *et al.* recently

proposed a model to calculate the grain boundary energy between any two misoriented grains [26] having FCC crystal structure taking into account the five physical parameters of misorientation. In the present work this new model is used; the three Euler angles defining the orientation of each grain are assigned randomly. The calculated data provided by Bulatov for the Ni system is used to approximate the grain boundary energy of Fe as their properties are quite similar to each other [34]. Because the approach proposed by Bulatov is limited to FCC systems, the coalescence model is only applicable to peritectic grades of steel.

Fig. 4(a) shows the output of a simulation, 125 mm<sup>3</sup> in size with an average grain size of 1000 μm for a Fe-0.16wt.%C alloy. The frequency of the calculated  $\gamma_{gb}$  between any two neighboring grains and the corresponding  $\Delta T_b$  based on the Bulatov's approach is plotted in Fig. 4(b). As can be seen,  $\gamma_{gb}$  ranges from 0.37 to 1.40 J/m<sup>2</sup>, which results in considerable undercooling required for coalescence, up to 145.2°C. The majority of the grain interfaces require undercooling greater than 100°C below the equilibrium solidus before coalescence occurs. The results also show that the proportion of negative coalescence undercoolings is ~ 0.9%, indicating that only a very small proportion of the grains are attractive to each other and promote the occurrence of solidification-related grain coalescence whereas the remainder are repulsive.

### 3. RESULTS AND DISCUSSION

The solidification of a binary Fe-C alloy is simulated below using the 3D meso-scale approach described above. The relevant material properties are listed in Table I. First, a description of the gradual formation of grain clusters during solidification is given to show the disappearance of liquid film between the neighboring two grains; Subsequently, the influence of carbon composition, cooling rate and grain size on the microstructure evolution and liquid channel width distribution is discussed.

#### 3.1 Grain Cluster Formation

The transition from individual solid grains surrounded by continuous liquid films to the formation of a single coherent solid cluster in a peritectic alloy containing 0.16 wt.% carbon is given in Fig. 5, where the domain is continuously cooled down at a cooling rate of 50°C/s. The coalescence undercoolings shown in Fig. 4 will be used as the input data for the grain cluster formation analysis.

Fig. 5(a) shows the morphology of grain clusters at different time (0.53 s, 1.07 s, 1.66 s, 2.63 s, 2.72 s and 2.79 s), where each color within the domain represents a single grain cluster that can be consisted of multiple/single grain(s). During initial solidification, the grains are separated by continuous liquid films, and the number of clusters is equal to the number of grains. As grains coalescence, the size of the largest grain cluster grows, reducing the number of liquid films between individual grains. Further, the liquid channel thicknesses will narrow to a few nanometers. Due to different misorientations between two distinct grains, the required coalescence undercoolings for bridging are different depending on their respective grain boundary energies. Based the energies given in Fig. 4(b), most of grains are repulsive and thus neighboring grains will only coalesce once the necessary undercooling temperature is reached. Fig. 5 (a2 – a5) all contain a solid fraction greater than 0.99; at such a high solid fraction, the presence of liquid films will increase hot tearing susceptibility when deformation is applied. Finally, all 125 grains coalescence to form a single grain cluster at 2.79 s, shown in Fig. 5(a6). At this point, the material is able

to sustain tensile deformation, having achieved mechanical coalescence. The evolution in grain clusters with time is quantified in Fig. 5(b). As can be seen, the speed of grain coalescence first increases because many of the grains require only a low coalescence undercooling, and then decreases because the final liquid films require significant undercooling to disappear.

### 3.2 *Microstructure Evolution*

#### 3.2.1 Influence of Carbon Content

The solidification morphology of various Fe-C alloys (non-peritectic: 0.07wt.%; hypo-peritectic: 0.12wt.%, peritectic: 0.16wt.% and hyper-peritectic: 0.18wt.%) is compared in Fig. 6 at three different temperatures. All simulations used the same cooling rate (50°C/s) and the same microstructure (500 μm average grain size). For the non-peritectic grade at high fraction solid, Fig. 6(a), it can be seen that many of the liquid channels are quite narrow although a few liquid pockets remain. As the grains solidify, they form a coherent solid (Fig. 6(a2)). The short freezing range results in limited hot tearing susceptibility. In comparison, a hypo-peritectic grade has a lower solid fraction at the same temperatures, and thus wider liquid channel widths, Fig. 6(b1), and multiple liquid pockets coexisting with the solid phase. At T=1492.22°C, a thin layer of austenite (highlighted in red) forms at δ/L interface, Fig. 6(b2), concurrently narrowing the remaining liquid channel width without enabling coalescence. Considerable liquid is required at this temperature to feed the shrinkage associated with solidification and the peritectic transformation. The austenite phase then continues to grow into the liquid and δ phases as temperature decreases, resulting in a microstructure shown in Fig. 6(b3). The solidification of peritectic and hyper-peritectic grades are shown in Fig. 6(c) and (d). With increasing carbon content, the liquid pockets increase in number and size. Compared with the microstructure of the peritectic grade shown in Fig. 6(c1), the hyper-peritectic grade (Fig. 6(d1)) tends to display thicker liquid channel widths enabling easy liquid feeding. As solidification proceeds, the peritectic phase is seen to form, Fig. 6(c2-c3) and (d2-d3). In the hyper-peritectic grade, a number of liquid pockets remain that could feed the shrinkage, whereas these pockets are largely absent in the peritectic grade and do not exist in the hypo-peritectic grade when the peritectic transformation occurs. Given the differences in composition, a greater amount of austenite forms in the hyper-peritectic grade as compared to the peritectic, and hypo-peritectic grades.

Fig. 7 quantifies the variation in liquid channels widths in the three peritectic grades just after the peritectic transformation has occurred, corresponding to Fig. 6(b3, c3, and d3). As can be seen, thicker liquid channel widths exist with higher carbon contents thus reducing hot tearing susceptibility at a given temperature as compared to the hypo-peritectic grade. Specifically, the majority of the liquid channel widths is ~28 μm for Fe-0.16wt.%C and ~2 μm for Fe-0.12wt.%C. Of course, the solid fraction is also lower for these cases but nevertheless the thin liquid channels make feeding very difficult at the point where liquid is needed to support the shrinkage associated with the peritectic transformation.

It should be noted that the equivalent liquid channels shown in Figures 6 represent the intra-dendritic liquid; as shown in Figure 3(b) the dendrite tip quickly reaches the grain edge under high (industrial) cooling rate conditions. Distinguishing between intra-dendritic liquid and the extra-dendritic liquid is of vital importance with respect to their relative effects on flow hindrance. For equivalent amount of liquid flow, the permeability of the intra-dendritic region will be much less in the extra-dendritic region

because of the additional presence of the dendrite. Conceptually, grains that solidify with a globular microstructure will have improved flow as compared to dendritic microstructure at equivalent solid fraction. Numerically, this is shown through the solid/liquid interfacial area concentration  $S_v$ . For dendritic structures the  $S_v$  term, related to the secondary arm spacing [35, 36], will be much larger than globular structures, which in turn results in a greater resistance to the liquid flow in the mushy zone as predicted by the Carman-Kozeny equation [37]. Lower permeability of the mushy zone indicates a poor feeding scenario and leads to higher pressure drop which would accelerate the formation of hot tearing. The feeding behavior of various semi-solid microstructures with both dendritic and globular morphology can be examined using the Darcy-Brinkman equation, and will be the subject of a future investigation.

### 3.2.2 Influence of Cooling Rate

Fig. 8 compares the meso-scale model predictions of the semi-solid microstructure for a Fe-0.07 wt.%C alloy solidified at three different cooling rates (25 °C/s, 50 °C/s and 75 °C/s), along with the corresponding distribution in liquid channel widths. All three images represent the same temperature, 1507.06°C. The secondary dendrite arm spacing used in the solidification model is cooling rate-dependent and will decrease with increasing cooling rate. The results demonstrate the ability of the solidification model to capture the differences in microstructure evolution under different cooling rates. At the temperature provided, the solid fraction decreases from 0.97 to 0.85 with increasing cooling rate. This is expected since higher cooling rates show a greater deviation from the equilibrium conditions leading to a decrease in the solid fraction at the same temperature compared with lower cooling rate. Further, a significant change in the liquid channel migration can be observed. A higher cooling rate of 75°C/s results in a structure with thicker liquid channel thicknesses as compared to the thinner liquid channels observed in the microstructure when the cooling rates are 25°C/s and 50°C/s. The localization of the liquid between the grains and the liquid pockets remain obvious when the cooling rate is high. The liquid channel widths shift from an average of 7.5 μm to ~30 μm with the increase in cooling rate.

### 3.2.3 Influence of Grain Size

Experimental measurement on grains size in steel indicates that the value ranges from the 400 to 800 μm near the surface of the cast slab, and 600 to 1600 μm at the bottom of oscillation marks [38]. The size of abnormally coarse grains, can be up to seven millimeters [39]. Regardless of the mechanism behind the formation of these large austenite grains, it is thought that they originate from large primary ferrite grains [40]. In this section, the influence of two different average grain sizes, 500 μm and 1000 μm, on the microstructure evolution of Fe-0.16 wt.%C is investigated. The cooling rates used for grain size of 500 μm and 1000 μm are 50 °C/s and 6.25 °C/s based on an empirical equation relating the average final grain size with cooling rate [41].

The simulated semi-solid microstructure and the liquid channel width variation at three different temperatures ( $T=1502.8$  °C,  $1497.8$  °C and  $1492.8$  °C) are shown in Fig. 9. First, independent of grain size, the solid fraction increases with a decrease in temperature along with the narrowing of the liquid channel widths as seen in both Fig. 9(a) and (b). At low solid fraction, the liquid channels vary considerably in size whereas at high solid fraction they are more likely to localize around a unique value. Second, the microstructure evolution clearly depends on the average grain size with numerous thin liquid

channels in the domain with 500  $\mu\text{m}$  grains and few large channels in the one with 1000  $\mu\text{m}$  grains at the same temperature. The quantification of channel width for both grain sizes show a Gaussian-like distribution at all temperatures although some discrepancy exists. As indicated in the figure, the number of facets in the domain with finer grain is about seven times as large as compared with the coarser domain, and the overall solid/liquid interfacial area associated with smaller grains is 7469.4  $\text{mm}^2$  which is much larger than large grains of 3389.3  $\text{mm}^2$ . Third, there is also a slight difference in the solid fraction of the two grain sizes for the same temperature. This is due to the statistical nature when placing grain nuclei inside a domain and performing a Voronoi tessellation. Higher cooling rates should also lead to a greater deviation from the equilibrium solidification, and cause lower overall solid fraction, also the effect is marginal between cooling rates of 6.25°C/s and 50°C/s

### 3.3 Hot Tearing Sensitivity Analysis

The main purpose of the present research has been to develop a meso-scale semi-solid framework for simulating the solidification of steel, and to provide quantitative information about the distribution of liquid channel widths and the proportion of each phase within individual grains for different physical and process parameters. It is well known that hypo-peritectic alloys are more sensitive to hot tearing as compared with other steel compositions. As shown in Figs. 6(b3), the liquid channel widths for this chemistry are much smaller than the ones found in peritectic and hyper-peritectic grades. The shrinkage caused by peritectic transformation requires additional liquid over top of the solidification shrinkage. Due to the thin liquid channel widths predicted to be present in the hypo-peritectic grade when the transformation occurs, the feeding through these liquid channels will be quite difficult. This is likely to increase hot tearing susceptibility. The present model thus demonstrates the underlying microstructure responsible for high hot tearing susceptibility in hypo-peritectic grades that has been previously experimentally reported [42]. Further, the results given in Fig. 8 indicate that larger cooling rates are more likely to lead to a lower overall solid fraction and thus wider liquid channels as compared with small cooling rates. These results are consistent with experimental findings that slow-cooled castings can sometimes be difficult to feed and thus prone to hot tearing. Finally, it is known that transverse cracks are usually found around abnormally coarse grains [1]. Based on Fig. 9, it is hypothesized that the larger interfacial area of small grains, and the resulting even distribution of liquid channels and coalesced channels provide better liquid feeding in response to tensile deformation [43].

## **4. CONCLUSIONS**

A new 3D meso-scale model based on the volume average method is proposed to predict the evolution in semi-solid microstructure of engineering alloys and consequently liquid film migration. This model is applied to Fe-C binary alloys having experiencing both primary solidification and the peritectic transformation. Solute diffusion within each phase (intra-dendritic liquid, extra-dendritic liquid,  $\delta$  phase and  $\gamma$  phase) is considered. The capability of the model in predicting solidification with both globular and dendritic structure has been demonstrated using a case study of two different cooling rates. At 0.1°C/s, a globular structure is predicted to form, while at 50°C/s a dendritic morphology is favored.

The model is then applied to correlate the semi-solid microstructure evolution to different physical and process parameters. The formation of austenite at increased carbon content, due to the peritectic transformation, will sharply increase the solid fraction and narrow the remaining liquid film widths. An increase in the cooling rate leads to higher deviation from equilibrium and thus lower solid fraction at a specified temperature which in turn reduces the occurrence of hot tearing. A domain with small grains will have thin liquid channels as compared to large grains, but there will be much more interfacial area thus more coalescence to resist hot tearing. Large grains are prone to hot tear due because of the difficulty in feeding through only a few liquid channels. Finally, the underlying microstructure leading to high hot tearing susceptibility of hypo-peritectic grades – namely liquid channels that are too thin to allow for feeding to compensate the volume change associated with the peritectic transformation – is identified.

## 5. ACKNOWLEDGEMENTS

The authors wish to thank the Natural Sciences and Engineering Research Council of Canada (NSERC) and the McMaster Steel Research Centre for financial support. Stimulating discussions with Dr. Miha Založnik at Université de Lorraine, France, and Dr. Brian Thomas at Colorado School of Mines, USA, are gratefully acknowledged.

## 6. TABLES AND FIGURES

Fig. 1. Various geometries of the 3D meso-scale model: (a) 3D Voronoi tessellation consisting of 27 grains each colored by a different grayscale value; (b) a single Voronoi grain; (c) polyhedral element, (d) tetrahedral element, (e) semi-solid domain with 1000 grains at the solid fraction 0.81. In (e) the liquid is colored black, while the delta ferrite grains are colored in gray. Note that the amount of remaining liquid within each grain is represented by the channel thickness.

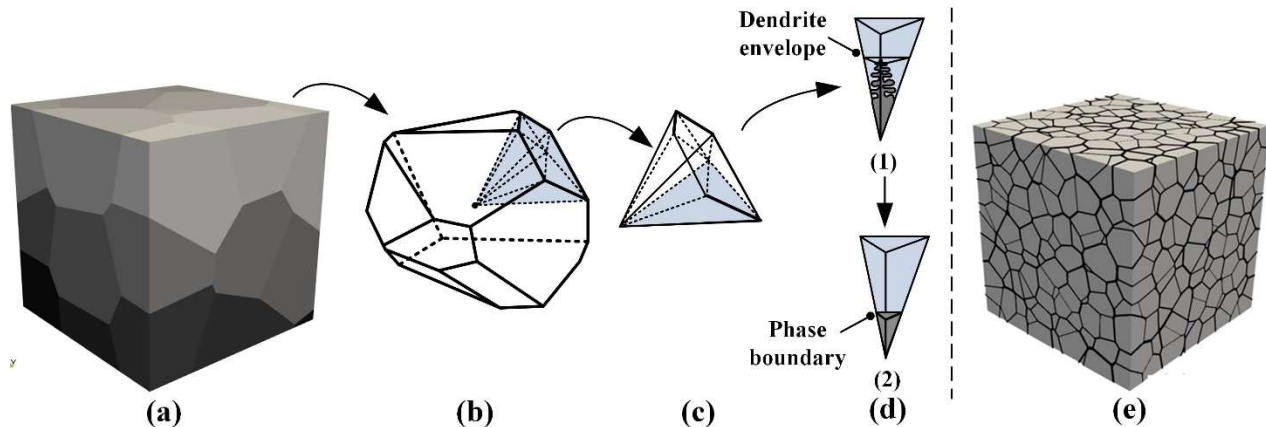


Fig. 2. Schematic diagram showing (a) primary solidification and (b) primary solidification plus peritectic transformation. The images (1), (2), and (3) show the actual dendritic structure, equivalent structure for the volume average model, and the geometric structure for the meso-scale model. The grey, red, and white regions indicate the  $\delta$ ,  $\gamma$  and  $l$  regions. The dotted red line denotes the dendrite envelope.

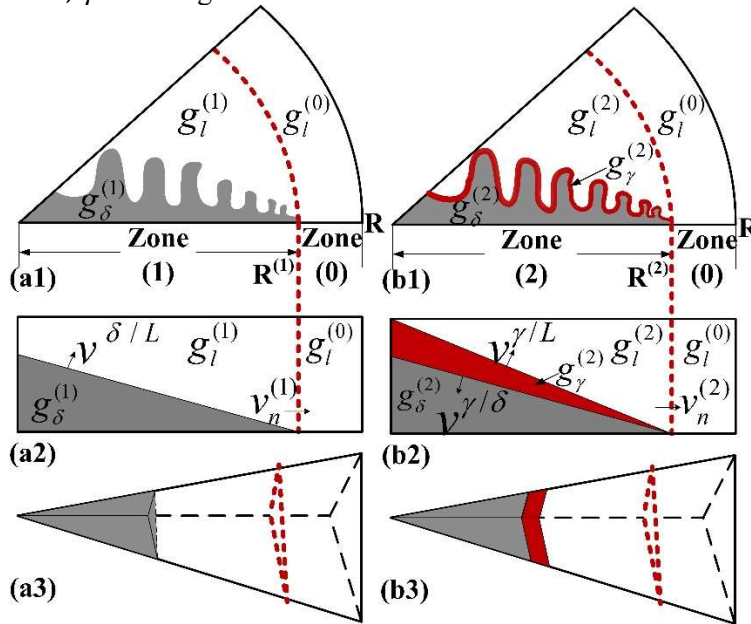


Fig. 3. Evolution of liquid, solid- $\delta$  and dendrite envelope fraction of a single grain for a Fe-0.07 wt.% C alloy cooling at (a)  $0.1^\circ\text{C/s}$  and (b)  $50^\circ\text{C/s}$ . A grain radius of  $100\ \mu\text{m}$  and a secondary arm spacing of  $20\ \mu\text{m}$  are assumed in both cases.

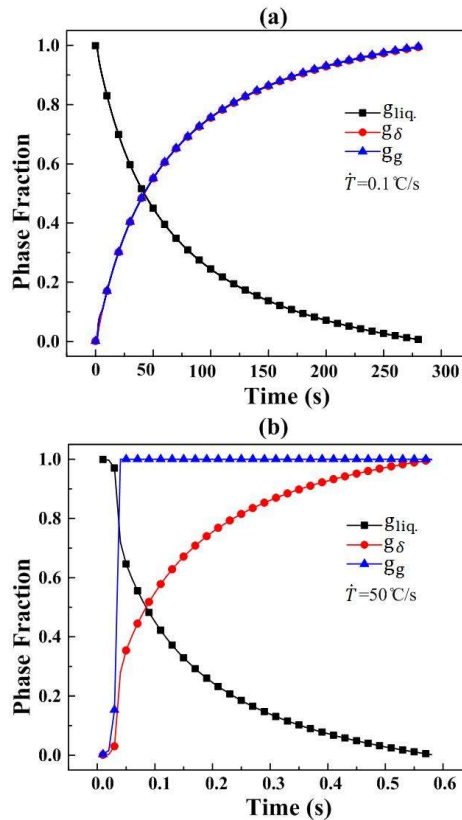


Fig. 4. (a) Meso-scale simulation domain containing 125 equiaxed grains with different orientations; (b) grain boundary energy and coalescence undercooling distributions used in the multi-physics model for a Fe-0.16wt.% C alloy as proposed by Bulatov et al.[26].

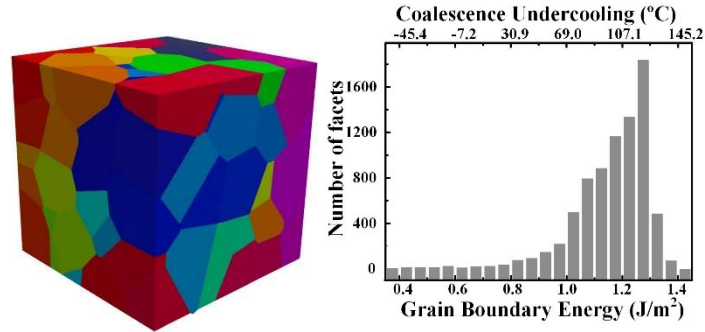


Fig. 5. Simulation domain (5mm×5mm×5mm) containing 125 grains for a Fe-0.16wt.%C alloy: (a) coalescence of grain clusters at different time; (b) evolution of the number of grain clusters as a function of time.

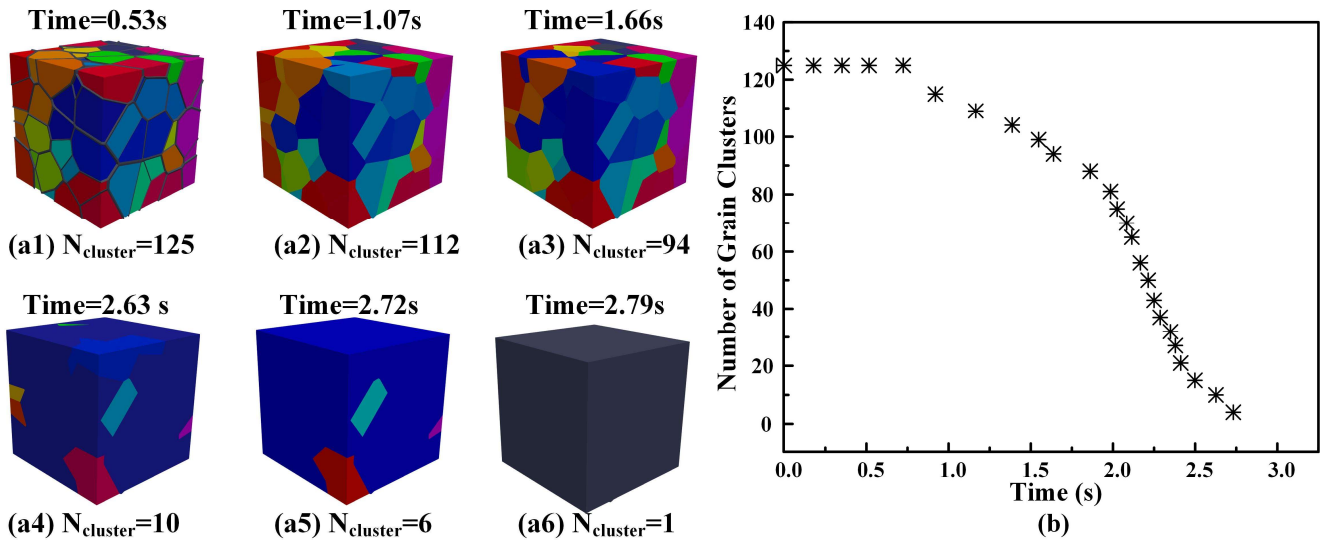


Fig. 6. 2D Cross-sections from the 3D meso-scale solidification model of steel consisting of 1000 grains and a total domain size of 125 mm<sup>3</sup>. (a-d) represent simulations with different carbon compositions, each for three different temperatures. (I-III) presents three different temperatures of 1507.1°C, 1492.2°C and 1491.8°C, respectively. Note that  $g_{L\_extra} \sim 0$ .

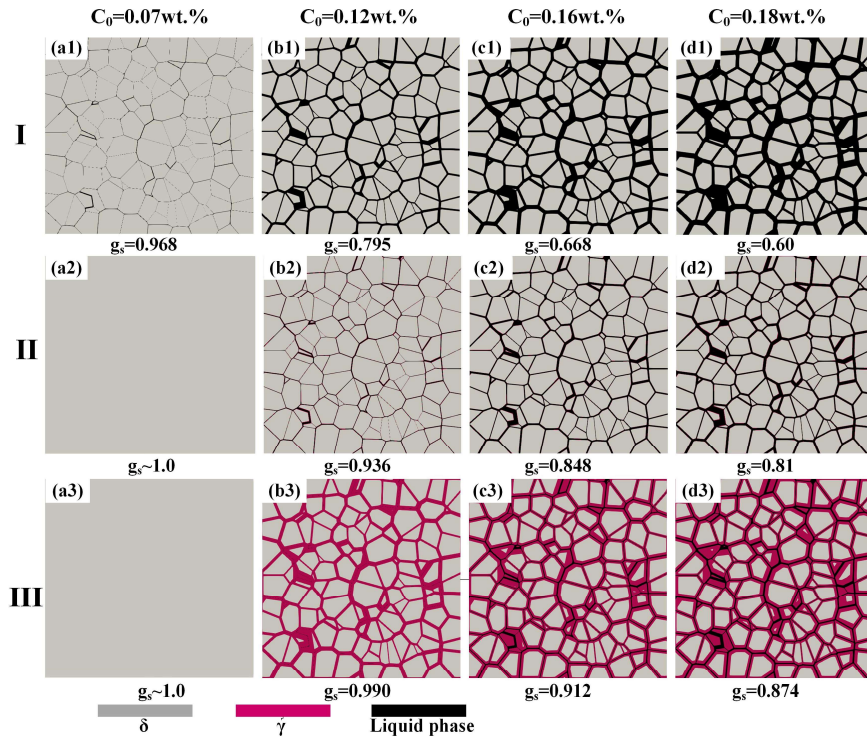


Fig. 7. The distribution in liquid channel widths for cases (b3), (c3), and (d3) from Figure 6 corresponding to compositions of 0.12wt.%, 0.16wt.%, and 0.18wt.% C.

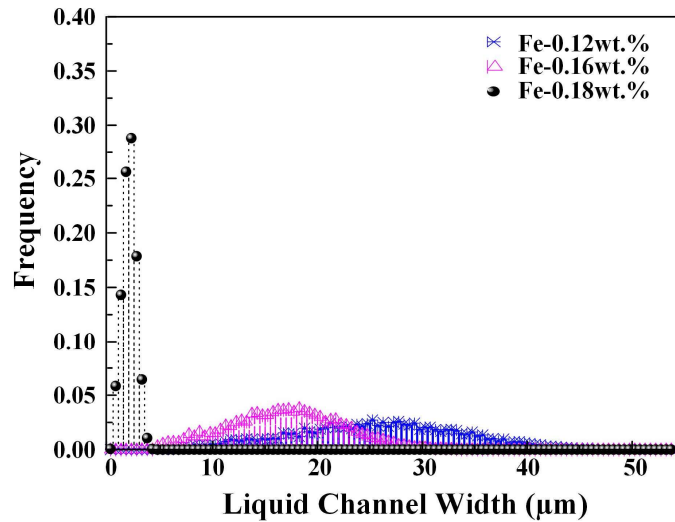


Fig. 8. The evolution of semi-solid microstructure and the liquid channel thickness within the domain size of 125 mm<sup>3</sup> consisting of 1000 grains for a Fe-0.07 wt.%C alloy at T=1507.06 °C under different cooling rates: (a) 25 °C/s; (b) 50 °C/s and (c) 75 °C/s. Note that  $g_{l\_extra} \sim 0$ .

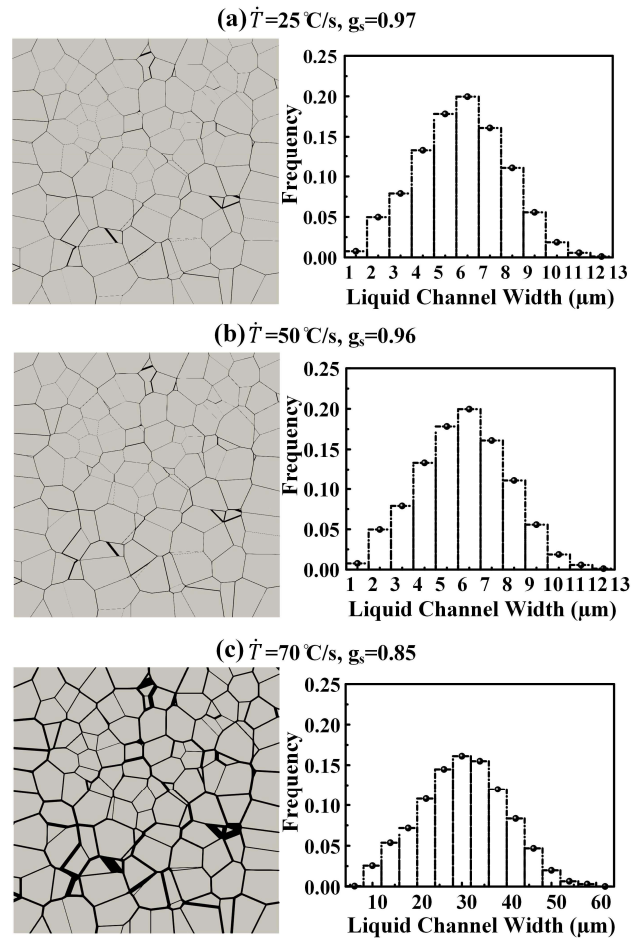


Fig. 9. The evolution of liquid channel width at different temperatures within the domain size of  $125 \text{ mm}^3$  for a Fe-0.16 wt.%C alloy consisting grains with average grain size of: (a)  $500 \mu\text{m}$ ; (b)  $1000 \mu\text{m}$ . Note that  $g_{l\_extra} \sim 0$ .

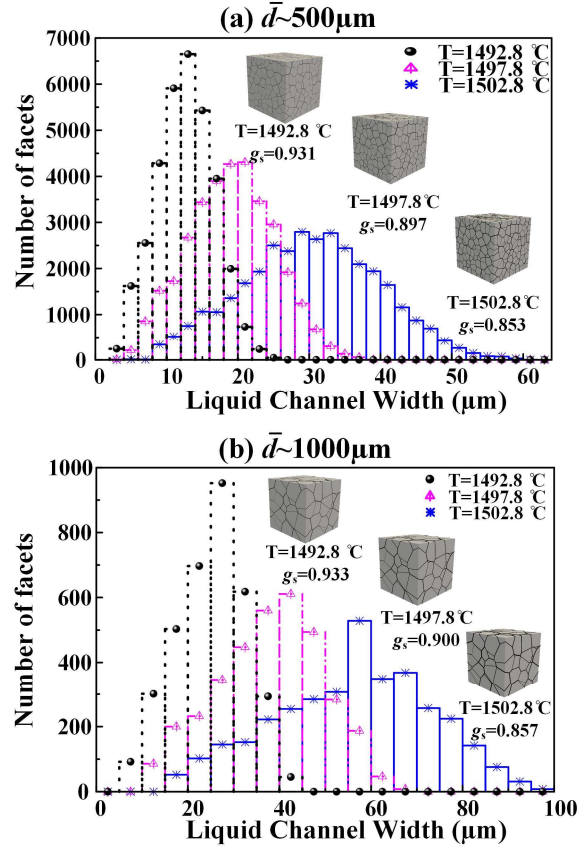


Table I. List of parameters used in the simulation for Fe-C alloy [44-48]

Property	
$\Delta S_f (\text{J K}^{-1} \text{m}^{-3})$	$1.07 \times 10^6$
$\eta (\text{nm})$	5
$\gamma_{sl} (\text{J m}^{-2})$	0.319
$D_l (\text{m}^2 \text{s}^{-1})$	$2.0 \times 10^{-8}$
$D_\delta (\text{m}^2 \text{s}^{-1})$	$6.0 \times 10^{-9}$
$D_\gamma (\text{m}^2 \text{s}^{-1})$	$1.0 \times 10^{-9}$
$\Gamma (\text{m K})$	$1.9 \times 10^{-7}$
$k$	0.17
$T_m (\text{°C})$	1538
$T_p (\text{°C})$	1493
$m_l (\text{K wt frac}^{-1})$	-84.90

## REFERENCES

- [1] E.S. Szekeres, A review of strand casting factors affecting transverse cracking, 2002, pp. 324-338.
- [2] H. Tsai, H. Yin, M. Lowry, S. Morales, Analysis of transverse corner cracks on slabs and countermeasures, *Iron & steel technology* 3(7) (2006) 23-31.
- [3] R. Mišičko, M. Fujda, S. Fedáková, D. Fedáková, S. Szekeres, Further Study of the „Blown Grains “Condition, *AlSTech*, 2012.
- [4] J. Sengupta, H.-J. Shin, B. Thomas, S.-H. Kim, Micrograph evidence of meniscus solidification and sub-surface microstructure evolution in continuous-cast ultralow-carbon steels, *Acta materialia* 54(4) (2006) 1165-1173.
- [5] E. Takeuchi, J. Brimacombe, Effect of oscillation-mark formation on the surface quality of continuously cast steel slabs, *Metallurgical Transactions B* 16(3) (1985) 605-625.
- [6] J. Brimacombe, K. Sorimachi, Crack formation in the continuous casting of steel, *metallurgical and materials transactions B* 8(2) (1977) 489-505.
- [7] W. Pellini, Strain theory of hot tearing, *Foundry* 80(11) (1952) 125-133.
- [8] M. Sistaninia, A. Phillion, J.-M. Drezet, M. Rappaz, Simulation of semi-solid material mechanical behavior using a combined discrete/finite element method, *Metallurgical and Materials Transactions A* 42(1) (2011) 239-248.
- [9] I. Farup, J.-M. Drezet, M. Rappaz, In situ observation of hot tearing formation in succinonitrile-acetone, *Acta materialia* 49(7) (2001) 1261-1269.
- [10] T. Clyne, G. Davies, Influence of composition on solidification cracking susceptibility in binary alloy systems, *British Foundryman* 74 (1981) 65-73.
- [11] J. Drezet, M. Gremaud, R. Graf, M. Gaumann, A new hot tearing criterion for steel, *Proceedings of the 4th European Continuous Casting Conference*, IOM communications, Birmingham, UK, 2002, pp. 755-763.
- [12] T. Koshikawa, M. Bellet, C.-A. Gandin, H. Yamamura, M. Bobadilla, Study of Hot Tearing During Steel Solidification Through Ingot Punching Test and Its Numerical Simulation, *Metallurgical and Materials Transactions A* 47(8) (2016) 4053-4067.
- [13] N. Prokhorov, Resistance to hot tearing of cast metals during solidification, *Russian castings production* 2(2) (1962) 172-175.
- [14] A. Yamanaka, K. Nakajima, K. Yasumoto, H. Kawashima, K. Nakai, Measurement of critical strain for solidification cracking, *Modelling of Casting, Welding and Advanced Solidification Processes V* (1991) 279-284.
- [15] M. Sistaninia, A. Phillion, J.-M. Drezet, M. Rappaz, A 3-D coupled hydromechanical granular model for simulating the constitutive behavior of metallic alloys during solidification, *Acta Materialia* 60(19) (2012) 6793-6803.
- [16] V. Mathier, A. Jacot, M. Rappaz, Coalescence of equiaxed grains during solidification, *Modelling and simulation in materials science and engineering* 12(3) (2004) 479-490.
- [17] S. Vernede, J.A. Dantzig, M. Rappaz, A mesoscale granular model for the mechanical behavior of alloys during solidification, *Acta Materialia* 57(5) (2009) 1554-1569.
- [18] S. Terzi, L. Salvo, M. Suéry, N. Limodin, J. Adrien, E. Maire, Y. Pannier, M. Bornert, D. Bernard, M. Felberbaum, In situ X-ray tomography observation of inhomogeneous deformation in semi-solid aluminium alloys, *Scripta Materialia* 61(5) (2009) 449-452.
- [19] H.Z. Rajani, A. Phillion, A mesoscale solidification simulation of fusion welding in aluminum–magnesium–silicon alloys, *Acta Materialia* 77 (2014) 162-172.
- [20] H.Z. Rajani, A. Phillion, 3D multi-scale multi-physics modelling of hot cracking in welding, *Materials & Design* 144 (2018) 45-54.
- [21] M. Rappaz, P. Thevoz, Solute diffusion model for equiaxed dendritic growth, *Acta Metallurgica* 35(7) (1987) 1487-1497.
- [22] C. Wang, C. Beckermann, A multiphase solute diffusion model for dendritic alloy solidification, *Metallurgical and Materials Transactions A* 24(12) (1993) 2787-2802.
- [23] D. Tournet, C.-A. Gandin, A generalized segregation model for concurrent dendritic, peritectic and eutectic solidification, *Acta Materialia* 57(7) (2009) 2066-2079.

- [24] D. Tournet, C.-A. Gandin, T. Volkman, D.M. Herlach, Multiple non-equilibrium phase transformations: Modeling versus electro-magnetic levitation experiment, *Acta Materialia* 59(11) (2011) 4665-4677.
- [25] D. Tournet, G. Reinhart, C.-A. Gandin, G.N. Iles, U. Dahlborg, M. Calvo-Dahlborg, C.M. Bao, Gas atomization of Al-Ni powders: Solidification modeling and neutron diffraction analysis, *Acta Materialia* 59(17) (2011) 6658-6669.
- [26] V.V. Bulatov, B.W. Reed, M. Kumar, Grain boundary energy function for fcc metals, *Acta Materialia* 65 (2014) 161-175.
- [27] H. Zhang, C.-A. Gandin, K. Nakajima, J. He, A multiphase segregation model for multicomponent alloys with a peritectic transformation, IOP Publishing, 2012, p. 012063.
- [28] W. Kurz, B. Giovanola, R. Trivedi, Theory of microstructural development during rapid solidification, *Acta metallurgica* 34(5) (1986) 823-830.
- [29] Y. Feng, A.B. Phillion, A 3D Meso-Scale Solidification Model for Steels, 2018 AISTech Conference, Philadelphia, PA, 2018.
- [30] M. Rappaz, A. Jacot, W.J. Boettinger, Last-stage solidification of alloys: Theoretical model of dendrite-arm and grain coalescence, *Metallurgical and Materials Transactions A* 34(3) (2003) 467-479.
- [31] S. Vernede, P. Jarry, M. Rappaz, A granular model of equiaxed mushy zones: Formation of a coherent solid and localization of feeding, *Acta Materialia* 54(15) (2006) 4023-4034.
- [32] M. Sistaninia, Prediction of hot tearing formation in metallic alloys using a granular approach, (2013).
- [33] S. Vernède, M. Rappaz, A simple and efficient model for mesoscale solidification simulation of globular grain structures, *Acta materialia* 55(5) (2007) 1703-1710.
- [34] H. Beladi, N.T. Nuhfer, G.S. Rohrer, The five-parameter grain boundary character and energy distributions of a fully austenitic high-manganese steel using three dimensional data, *Acta materialia* 70 (2014) 281-289.
- [35] M. El-Bealy, B.G. Thomas, Prediction of dendrite arm spacing for low alloy steel casting processes, *Metallurgical and materials transactions B* 27(4) (1996) 689-693.
- [36] C. Wang, S. Ahuja, C. Beckermann, H. De Groh, Multiparticle interfacial drag in equiaxed solidification, *Metallurgical and Materials Transactions B* 26(1) (1995) 111-119.
- [37] P.C. Carman, Fluid flow through granular beds, *Trans. Inst. Chem. Eng.* 15 (1937) 150-166.
- [38] B. Weisgerber, K. Harste, W. Bleck, Phenomenological description of the surface morphology and crack formation of continuously cast peritectic steel slabs, *steel research international* 75(10) (2004) 686-692 %@ 1611-3683.
- [39] C. Bernhard, J. Reiter, H. Presslinger, A model for predicting the austenite grain size at the surface of continuously-cast slabs, *Metallurgical and Materials Transactions B* 39(6) (2008) 885-895 %@ 1073-5615.
- [40] R. Dippenaar, C. Bernhard, S. Schider, G. Wieser, Austenite grain growth and the surface quality of continuously cast steel, *Metallurgical and Materials Transactions B* 45(2) (2014) 409-418.
- [41] J.A. Dantzig, M. Rappaz, Solidification, EPFL press 2009.
- [42] P. Presoly, R. Pierer, C. Bernhard, Identification of defect prone peritectic steel grades by analyzing high-temperature phase transformations, *Metallurgical and Materials Transactions A* 44(12) (2013) 5377-5388.
- [43] A. Phillion, S. Vernede, M. Rappaz, S. Cockcroft, P. Lee, Prediction of solidification behaviour via microstructure models based on granular structures, *International Journal of Cast Metals Research* 22(1-4) (2009) 240-243.
- [44] J. Chipman, Thermodynamics and phase diagram of the Fe-C system, *Metallurgical and Materials Transactions B* 3(1) (1972) 55-64 %@ 1073-5615.
- [45] W. Kurz, D.J. Fisher, Fundamentals of solidification, trans tech publications Aedermannsdorf, Switzerland 1986.
- [46] M. ODE, S.G. KIM, W.T. KIM, T. SUZUKI, Numerical simulation of peritectic reaction in Fe-C alloy using a multi-phase-field model, *ISIJ international* 45(1) (2005) 147-149.
- [47] D.Y. Sun, M. Asta, J.J. Hoyt, Crystal-melt interfacial free energies and mobilities in fcc and bcc Fe, *Physical Review B* 69(17) (2004) 174103.
- [48] M. Yamazaki, Y. Natsume, H. Harada, K. Ohsasa, Numerical simulation of solidification structure formation during continuous casting in Fe-0.7 mass% C alloy using cellular automaton method, *ISIJ international* 46(6) (2006) 903-908.